

Full-range, high-speed, high-resolution 1- μm spectral-domain optical coherence tomography using BM-scan for volumetric imaging of the human posterior eye

Shuichi Makita^{1*}, Tapio Fabritius^{1,2}, Yoshiaki Yasuno¹

¹Computational Optics Group in the University of Tsukuba, 1-1-1 Tennodai, Tsukuba, Ibaraki, 3058573, Japan.

²Optoelectronics and Measurement Techniques Laboratory, University of Oulu, 90014 University of Oulu, Finland.

makita@optlab2.bk.tsukuba.ac.jp

Abstract: An alternative optical coherence tomography (OCT) to clinical ophthalmic 830 nm spectral-domain OCTs (SD-OCT) is demonstrated. An axial resolution of 7.4 μm , ranging depth of 4.2 mm in tissue, sensitivity of 98.5 dB, and detection speed of 38,300 axial scans/s have been achieved. These are comparable or superior to those of recently commercially available ophthalmic 830 nm SD-OCTs in clinics. In addition, fast volumetric imaging for the *in vivo* human posterior eye with high-contrast of the choroid is achieved. A broadband 1.04 μm light source enables the high-contrast and high resolution imaging of the retina and choroid. The ranging depth is extended by applying a full-range imaging method with an electro-optic modulator (BM-scan method). A prototype high-speed InGaAs line scan camera with 1024 pixels is used. A newly reported sensitivity improvement property of the BM-scan method demonstrates a sensitivity enhancement of 5.1 dB. We also introduce a newly developed resampling calibration method of spectrum that is independent of the intrinsic dispersion mismatch of the interferometer. The three-dimensional structure of the *in vivo* human optic nerve head with a very deep cupping is successfully visualized.

© 2008 Optical Society of America

OCIS codes: (170.4500) Optical coherence tomography; (170.4470) Ophthalmology; (170.3880) Medical and biological imaging; (120.5050) Phase measurement.

References and links

1. A. Fercher, C. Hitzenberger, G. Kamp, and S. El-Zaiat, "Measurement of intraocular distances by backscattering spectral interferometry," *Opt. Commun.* **117**, 43–48 (1995).
2. G. Häusler and M. W. Lindner, "'Coherence Radar' and 'Spectral Radar'—New Tools for Dermatological Diagnosis," *J. Biomed. Opt.* **3**, 21–31 (1998).
3. T. Mitsui, "Dynamic range of optical reflectometry with spectral interferometry," *Jpn. J. Appl. Phys.* **38**, 6133–6137 (1999).
4. R. Leitgeb, C. Hitzenberger, and A. Fercher, "Performance of fourier domain vs. time domain optical coherence tomography," *Opt. Express* **11**, 889–894 (2003), <http://www.opticsexpress.org/abstract.cfm?id=71990>.
5. J. F. de Boer, B. Cense, B. H. Park, M. C. Pierce, G. J. Tearney, and B. E. Bouma, "Improved signal-to-noise ratio in spectral-domain compared with time-domain optical coherence tomography," *Opt. Lett.* **28**, 2067–2069 (2003).

6. M. Choma, M. Sarunic, C. Yang, and J. Izatt, "Sensitivity advantage of swept source and Fourier domain optical coherence tomography," *Opt. Express* **11**, 2183–2189 (2003), <http://www.opticsexpress.org/abstract.cfm?id=78787>.
7. N. Nassif, B. Cense, B. H. Park, S. H. Yun, T. C. Chen, B. E. Bouma, G. J. Tearney, and J. F. de Boer, "In vivo human retinal imaging by ultrahigh-speed spectral domain optical coherence tomography," *Opt. Lett.* **29**, 480–482 (2004).
8. S. Alam, R. J. Zawadzki, S. Choi, C. Gerth, S. S. Park, L. Morse, and J. S. Werner, "Clinical Application of Rapid Serial Fourier-Domain Optical Coherence Tomography for Macular Imaging," *Ophthalmology* **113**, 1425–1431 (2006).
9. M. Hangai, Y. Ojima, N. Gotoh, R. Inoue, Y. Yasuno, S. Makita, M. Yamanari, T. Yatagai, M. Kita, and N. Yoshimura, "Three-dimensional Imaging of Macular Holes with High-speed Optical Coherence Tomography," *Ophthalmology* **114**, 763–773 (2007).
10. M. Hammer, A. Roggan, D. Schweitzer, and G. Müller, "Optical properties of ocular fundus tissues—an in vitro study using the double-integrating-sphere technique and inverse Monte Carlo simulation." *Phys. Med. Biol.* **40**, 963–978 (1995).
11. B. Povazay, K. Bizheva, B. Hermann, A. Unterhuber, H. Sattmann, A. Fercher, W. Drexler, C. Schubert, P. Ahnelt, M. Mei, R. Holzwarth, W. Wadsworth, J. Knight, and P. S. J. Russell, "Enhanced visualization of choroidal vessels using ultrahigh resolution ophthalmic OCT at 1050 nm," *Opt. Express* **11**, 1980–1986 (2003), <http://www.opticsexpress.org/abstract.cfm?URI=oe-11-17-1980>.
12. A. Unterhuber, B. Povazay, B. Hermann, H. Sattmann, A. Chavez-Pirson, and W. Drexler, "In vivo retinal optical coherence tomography at 1040 nm-enhanced penetration into the choroid," *Opt. Express* **13**, 3252–3258 (2005), <http://www.opticsexpress.org/abstract.cfm?URI=OPEX-13-9-3252>.
13. E. C. Lee, J. F. de Boer, M. Mujat, H. Lim, and S. H. Yun, "In vivo optical frequency domain imaging of human retina and choroid," *Opt. Express* **14**, 4403–4411 (2006), <http://www.opticsexpress.org/abstract.cfm?id=89920>.
14. Y. Yasuno, Y. Hong, S. Makita, M. Yamanari, M. Akiba, M. Miura, and T. Yatagai, "In vivo high-contrast imaging of deep posterior eye by 1- μ m swept source optical coherence tomography and scattering optical coherence angiography," *Opt. Express* **15**, 6121–6139 (2007), <http://www.opticsexpress.org/abstract.cfm?id=134551>.
15. R. Huber, D. C. Adler, V. J. Srinivasan, and J. G. Fujimoto, "Fourier domain mode locking at 1050 nm for ultrahigh-speed optical coherence tomography of the human retina at 236,000 axial scans per second." *Opt. Lett.* **32**, 2049–2051 (2007).
16. B. Povazay, B. Hermann, A. Unterhuber, B. Hofer, H. Sattmann, F. Zeiler, J. E. Morgan, C. Falkner-Radler, C. Glittenberg, S. Blinder, and W. Drexler, "Three-dimensional optical coherence tomography at 1050 nm versus 800 nm in retinal pathologies: enhanced performance and choroidal penetration in cataract patients," *J. Biomed. Opt.* **12**, 041211 (pages 7) (2007).
17. G. Hale and M. Querry, "Optical constants of water in the 200-nm to 200- μ m wavelength region," *Appl. Opt.* **12**, 555–563 (1973).
18. Y. Wang, J. Nelson, Z. Chen, B. Reiser, R. Chuck, and R. Windeler, "Optimal wavelength for ultrahigh-resolution optical coherence tomography," *Opt. Express* **11**, 1411–1417 (2003), <http://www.opticsexpress.org/abstract.cfm?URI=oe-11-12-1411>.
19. M. Wojtkowski, A. Kowalczyk, R. Leitgeb, and A. Fercher, "Full range complex spectral optical coherence tomography technique in eye imaging," *Opt. Lett.* **27**, 1415–1417 (2002).
20. A. Bachmann, R. Leitgeb, and T. Lasser, "Heterodyne Fourier domain optical coherence tomography for full range probing with high axial resolution," *Opt. Express* **14**, 1487–1496 (2006), <http://www.opticsexpress.org/abstract.cfm?id=88060>.
21. Y. Yasuno, S. Makita, T. Endo, G. Aoki, H. Sumimura, M. Itoh, and T. Yatagai, "One-shot-phase-shifting Fourier domain optical coherence tomography by reference wavefront tilting," *Opt. Express* **12**, 6184–6191 (2004), <http://www.opticsexpress.org/abstract.cfm?id=81980>.
22. M. A. Choma, C. Yang, and J. A. Izatt, "Instantaneous quadrature low-coherence interferometry with 3 \times 3 fiber-optic couplers," *Opt. Lett.* **28**, 2162–2164 (2003).
23. B. Vakoc, S. Yun, G. Tearney, and B. Bouma, "Elimination of depth degeneracy in optical frequency-domain imaging through polarization-based optical demodulation," *Opt. Lett.* **31**, 362–364 (2006).
24. Y. K. Tao, M. Zhao, and J. A. Izatt, "High-speed complex conjugate resolved retinal spectral domain optical coherence tomography using sinusoidal phase modulation," *Opt. Lett.* **32**, 2918–2920 (2007).
25. A. Vakhtin, K. Peterson, and D. Kane, "Resolving the complex conjugate ambiguity in Fourier-domain OCT by harmonic lock-in detection of the spectral interferogram," *Opt. Lett.* **31**, 1271–1273 (2006).
26. Y. Yasuno, S. Makita, T. Endo, G. Aoki, M. Itoh, and T. Yatagai, "Simultaneous B-M-mode scanning method for real-time full-range Fourier domain optical coherence tomography," *Appl. Opt.* **45**, 1861–1865 (2006).
27. R. K. Wang, "In vivo full range complex Fourier domain optical coherence tomography," *Appl. Phys. Lett.* **90**, 054,103 (2007).
28. B. Baumann, M. Pircher, E. Götzinger, and C. K. Hitzenberger, "Full range complex spectral domain optical coherence tomography without additional phase shifters," *Opt. Express* **15**, 13,375–13,387 (2007), <http://www.opticsexpress.org/abstract.cfm?URI=oe-15-20-13375>.

29. R. A. Leitgeb, R. Michaely, T. Lasser, and S. C. Sekhar, "Complex ambiguity-free Fourier domain optical coherence tomography through transverse scanning," *Opt. Lett.* **32**, 3453–3455 (2007).
30. L. An and R. K. Wang, "Use of a scanner to modulate spatial interferograms for in vivo full-range Fourier-domain optical coherence tomography," *Opt. Lett.* **32**, 3423–3425 (2007).
31. S. Vergnole, G. Lamouche, and M. L. Dufour, "Artifact removal in Fourier-domain optical coherence tomography with a piezoelectric fiber stretcher," *Opt. Lett.* **33**, 732–734 (2008).
32. American National Standard Institute, *American National Standard for Safe Use of Lasers: ANSI Z136.1* (Laser Institute of America, Orlando, Florida, 2000).
33. Y. Yasuno, V. D. Madjarova, S. Makita, M. Akiba, A. Morosawa, C. Chong, T. Sakai, K.-P. Chan, M. Itoh, and T. Yatagai, "Three-dimensional and high-speed swept-source optical coherence tomography for in vivo investigation of human anterior eye segments," *Opt. Express* **13**, 10,652–10,664 (2005). <http://www.opticsexpress.org/abstract.cfm?id=86669>,
34. S. Yun, G. Tearney, B. Bouma, B. Park, and J. de Boer, "High-speed spectral-domain optical coherence tomography at 1.3 μm wavelength," *Opt. Express* **11**, 3598–3604 (2003). <http://www.opticsexpress.org/abstract.cfm?id=78225>,
35. M. Szkulmowski, A. Szkulmowska, T. Bajraszewski, A. Kowalczyk, and M. Wojtkowski, "Flow velocity estimation using joint Spectral and Time domain Optical Coherence Tomography," *Opt. Express* **16**, 6008–6025 (2008). <http://www.opticsexpress.org/abstract.cfm?URI=oe-16-9-6008>,
36. E. J. McDowell, X. Cui, Z. Yaqoob, and C. Yang, "A generalized noise variance analysis model and its application to the characterization of 1/f noise," *Opt. Express* **15**, 3833–3848 (2007). <http://www.opticsexpress.org/abstract.cfm?URI=oe-15-7-3833>,
37. J. Greivenkamp and J. Bruning, "Phase shifting interferometries," in *Optical shop testing*, D. Malacara, ed., Wiley Series in Pure and Applied Optics, 2nd ed., chap. 14, pp. 501–598 (John Wiley & Sons Inc., 1992).

1. Introduction

The recent developments in spectral-domain optical coherence tomography (SD-OCT) [1, 2] achieve high-speed three-dimensional imaging due to its superior sensitivity than those of time-domain techniques [3, 4, 5, 6]. This modality enables high-speed 3D retinal imaging [7] and the precise morphological investigation of retinal pathologies [8, 9].

One of the limitations of the clinical OCT imaging of the human posterior eye is the absorption by water which is the main content of the transparent media, i.e., the aqueous humor and vitreous. To maximize the transmittance of light, a light source with an optical wavelength band of 830 nm which is located around the local minimum in the absorption coefficient of water is used for the OCT imaging of retinal pathologies. Therefore, the light is delivered to the posterior part of the eye efficiently. However, this wavelength band suffers from high absorption coefficients of pigmented tissues such as the retinal pigment epithelium (RPE) and the choroid [10]. Furthermore, the shorter wavelength is scattered more severely in tissues. These facts result in the low penetration of light into deep regions and the less imaging contrast.

According to several studies conducted to investigate the optimal wavelength band in ophthalmic OCT imaging, 1 μm wavelength band is suitable for high-sensitive and high-contrast imaging of the retina and deeper regions of the choroid [11, 12]. By using this wavelength band, high-contrast *in vivo* imaging beneath the RPE is demonstrated [13, 14, 15, 16]. Because this wavelength is longer than the wavelength band of 830 nm, the absorption coefficients of the ocular pigmented tissues decrease [10], while the absorption coefficient of water has a local minimum at a wavelength of 1.06 μm [17]. Furthermore, the depth-dependent broadening of the axial point spread function of the OCT images is suppressed due to low chromatic dispersion of water [18].

Currently, high-speed 1 μm OCT is achieved by employing the frequency domain detection technique with a wavelength-scanning light source—swept-source OCT (SS-OCT) [13, 14, 15]. However, the axial resolution is limited to approximately 10 μm in tissue. To clearly reveal the fine structures of the retina such as the RPE, inner/outer segment junction, and external limiting membrane which are related to diagnose retinal pathologies, a high axial resolution is preferred. Považay et al. have demonstrated 1 μm band SD-OCT with an axial resolution of $\sim 7 \mu\text{m}$ [16].

However, the imaging speed is slower than those of commercially available ophthalmic 830 nm SD-OCTs in clinics. In addition, its imaging depth range is limited into 1.7 mm since an InGaAs line scan camera with a small number of pixels is used. It cannot cover an entire deep cup of the optic nerve head (ONH) with and a height of a large elevation in retinal pathologies, such as severe age-related macular degeneration.

In SD-OCT, there are several factors which restrict its axial imaging range. The fraction of the axial range and resolution is restricted by the number of pixels; thus, high axial resolution and a small number of pixels result in short ranging depth. Furthermore, unwanted signals, which are the so-called a mirror image, dc, and autocorrelation artifacts, limit the axial imaging range into half. Because of the existence of these signals, the depth-resolved structural image cannot be located around zero-delay, which is the most sensitive region since the finite spectral resolution causes the depth dependent decay of the signal-to-noise ratio (SNR).

The solution of these problems is to resolve the complex ambiguity [19, 20, 21, 22, 23, 24, 25]. The mirror image, dc, and autocorrelation artifacts can be removed by obtaining the complex spectrum. Thus, the ranging depth becomes double and the images can be placed around zero-delay.

In this study, we demonstrate an alternative 1 μm SD-OCT to clinical ophthalmic 830 nm SD-OCTs. By using a broadband light source of 1 μm , imaging of the human posterior eye with a high-resolution and high-contrast in the choroid is enabled. A prototype of a high-speed InGaAs line scan camera is used and fast 3D volumetric imaging is achieved. To overcome the limited depth range due to the small number of the pixels, the BM-scan method [26, 27, 28, 29, 30, 31], which is one of full-range SD-OCT techniques, is used because of its simple configuration and high tolerance of phase-shift errors. In this method, phase modulation (M-scan) is applied to the reference beam while a mechanical scanner scans the sample beam laterally (B-scan); then, OCT image and its mirror image are separated in temporal frequency domain. For this BM-scan method, a discrete phase modulation is applied with the electro-optic modulator (EOM) to avoid the fringe washout. Volumetric posterior eye imaging is performed using this system. Three-dimensional structure of the ONH with deep cupping can be obtained which requires the deep ranging depth.

2. Full-range 1 μm SD-OCT system

2.1. Experimental setup

The system is based on the unbalanced Michelson interferometer, as shown in Fig. 1. By using a broadband 1 μm ASE light source (NP Photonics), posterior eye imaging can be achieved with high-penetration and a high resolution. The light source has a central wavelength of 1042 nm and a spectral width (FWHM) of 62 nm. The axial resolution was measured to be 7.4 μm in tissue. The light from the fiber-coupled light source is divided and delivered to the sample and reference arms by the 10/90 fiber coupler. In the sample arm, 10 % of the light is delivered to the retina via the customized retinal scanner based on 3D-OCT 1000 (Topcon Corp., Tokyo, Japan). The power of light incident on the cornea is 840 μW . This power is lower than the exposure limit prescribed by the ANSI safety standard, i.e., 1.68 mW at 1040 nm with duration of over 10 s [32]. The expected beam width on the retina is about 20 μm . For full-range imaging, the EOM is introduced in the reference arm to modulate the phase of the reference beam. The polarizer before the EOM extracts the polarization state of the reference beam parallel to the optic axis of the crystal in the EOM. The optical power of the reference beam is optimized by the variable neutral density filter in order to maximize the sensitivity of the system. The recombined light is resolved by the high-speed spectrometer using the collimator lens, transmission grating (1450 lp/mm, Wasatch Photonics Inc.), achromatic lens pair ($f = 300$ mm and 150 mm, assemble a composite lens with $f = 120$ mm), and a prototype of a high-speed InGaAs line scan camera

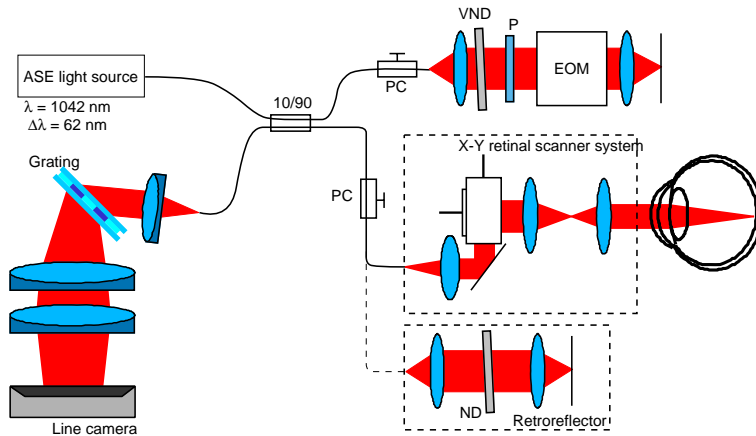


Fig. 1. The schematic diagram of the optical setup. VND: variable neutral density filter; ND: neutral density filter; and P: polarizer.

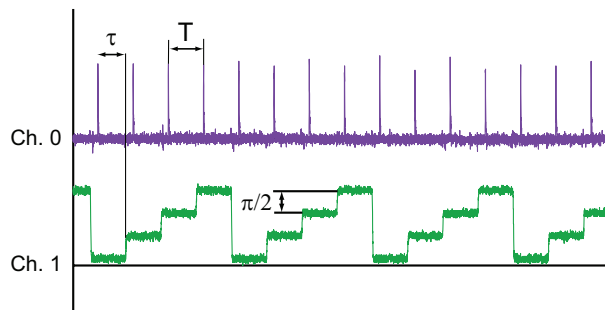


Fig. 2. Waveforms for driving and synchronizing the system. Ch.0: the TTL from the camera at the start of the integration and Ch.1: the waveform for phase modulation applied to the EOM.

(Hamamatsu Photonics K.K., Hamamatsu, Japan). The line scan camera has 1024 pixels with a pitch of $25 \mu\text{m}$ and a height of $100 \mu\text{m}$ and can be driven a line rate of up to 44.7 kHz. The data is transferred to a personal computer via Camera Link connection.

The waveforms to drive the system are shown in Fig. 2. The EOM is modulated with a discrete sawtooth waveform, and the update timing of applied voltage is synchronized to the end of the camera integration in order to minimize the reduction of the SNR due to the fringe washout. It is a four-step sawtooth waveform with a modulation depth of $3\pi/2$ radians. The phase offset between each step is $\pi/2$. It corresponds to the wrapped linearly increased phase modulation with a slope of $\pi/2$ radian/step. In the current setup, the integration time, τ , and the reset time of the capacitor of the camera are set to be $20.1 \mu\text{s}$ and $6 \mu\text{s}$; thus, the acquisition rate is $1/T = 38.3 \text{ kHz}$. The reset time is selected to avoid that the camera integrates during the EOM is unsettled. The scanning of the beam spot is applied simultaneously to this modulation. The ratio of scanning spacing to the beam spot size should be, at least, smaller than $\pi/8$ as mentioned in Sec. 4.

2.2. Spectrometer calibration with dispersion mismatched interferometer

SD-OCT requires the spectral interferometric fringe to be evenly sampled in terms of wavenumber in order to reconstruct the axial profile of the tissue with fast Fourier transform (FFT). In

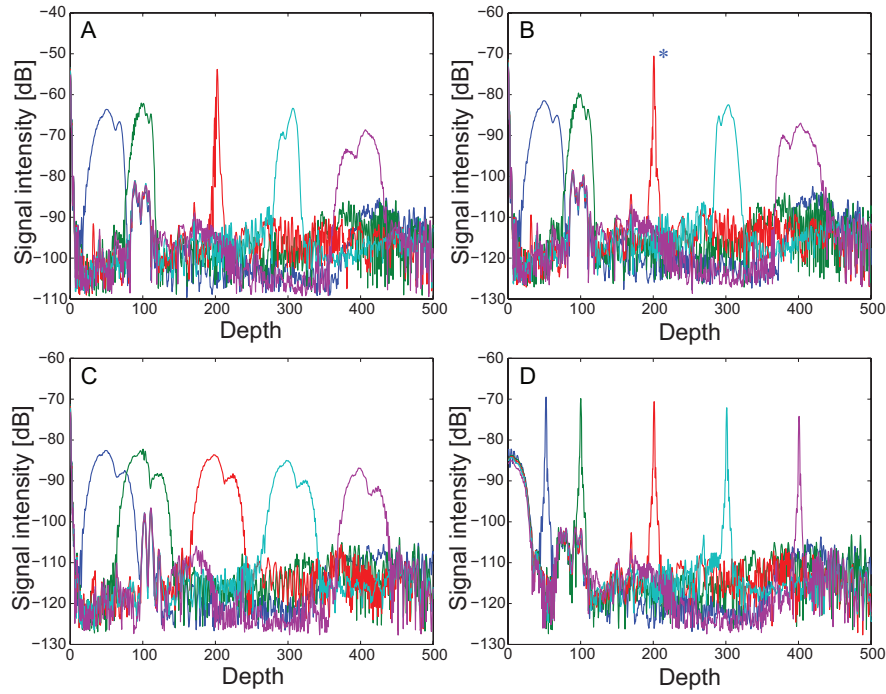


Fig. 3. The Fourier transform result of the raw spectrum (A); the axial profile with the previous method with a single calibration spectrum. The blue asterisk indicates the point spread function created from the spectrum which was utilized by the calibration. (B); the axial profile with the new method with two calibration spectra (C); and the axial profile obtained with the new resampling method and numerical dispersion compensation (D).

general, the detected interferometric spectra are resampled. We have developed a spectrum resampling method based on a phase of a pre-detected interferometric fringe with a single layered reflector as the sample [33]. However, it is based on the assumption that the dispersions of the sample and reference arms are balanced. Otherwise, the dispersion mismatch causes the wavelength dependent phase offset in the spectral fringe and adversely affects the resampling method.

The phase of the spectral interference signal is used in order to obtain the resampling points. A single reflective surface such as a mirror is placed on the sample arm of the interferometer, and the spectral signal is obtained with the spectrometer. The number of photoelectrons acquired by the line scan camera can be expressed as

$$\mathcal{N}[k(\xi_j)] = q\eta S[k(\xi_j)]\{P_s + P_r + 2\sqrt{P_r P_s} \cos[2k(\xi_j)z_0 + \Delta\phi_{CD}(k)]\}, \quad (1)$$

where k is the wavenumber; ξ_j , the position of each pixel on the line scan camera; q , the quantum efficiency of the camera; η , the diffraction efficiency of the spectrometer; P_s and P_r , the optical power of the sample and reference beams, respectively. The third term in parentheses denotes the interferometric signal. z_0 is the optical path length difference between the sample and reference arms at the central wavenumber k_0 . $\Delta\phi_{CD}(k)$ is the phase difference introduced by the wavelength-dependent optical path length difference. If there is no chromatic dispersion mismatch of higher than second order between the sample and reference arms, $\Delta\phi_{CD}(k)$ becomes proportional to k ; therefore, the previous algorithm [33] can be applied directly. How-

ever, if it is not, the spectrum resampling will be fail and the OCT signal will be broadened depending on the depth.

To cancel the dispersion mismatch effect, one additional reference spectrum with different axial position of the reflector is measured. The phase of this interferometric fringe can be described as $2k(\xi_j)z'_0 + \Delta\phi_{CD}(k)$. Since the dispersion mismatch is not changed in both cases, the phase offset of the fringes due to the system dispersion can be canceled out by subtracting both phases of the spectral fringes.

$$\begin{aligned}\Delta\phi(\xi_j) &= 2k(\xi_j)z_0 + \Delta\phi_{CD}(k) - (2k(\xi_j)z'_0 + \Delta\phi_{CD}(k)) \\ &= 2k(\xi_j)[z_0 - z'_0].\end{aligned}\quad (2)$$

Since the resulting spectral phase difference $\Delta\phi(\xi_j)$ changes linearly with the wavenumber k , it can be used to determine the resampling positions. In Fig. 3, the axial profiles of several depths of a reflector are shown. The profiles of directly Fourier transformed raw spectra exhibit broadening due to the nonlinear spacing of the spectra in k -space (Fig. 3A). Because of the dispersion mismatch of the system due to the unbalanced fiber length and different optical components, the broadening is not monotonically increased. The axial profiles obtained by the previous method (Fig. 3B) show a false calibration of the spectrometer nonlinearity, where the narrowest point spread function is achieved at around 200-th pixel. This is because the interference signal with a delay of ~ 200 -th pixel (blue asterisk) is used to decide the resampling points. By applying the new method, the profiles are equally broadened since only the effect of the dispersion mismatch remains (Fig. 3C). This shows that the new method is independent of the system dispersion mismatch. The axial profiles are sharpened in the entire axial range after automatic numerical dispersion compensation [14] (Fig. 3D).

2.3. Signal processing of full-range SD-OCT imaging

For full-range imaging, the complex spectrum is obtained by employing the BM-scan method [26] and by applying conventional SD-OCT processing. A schematic diagram of the processing method is shown in Fig. 4. After subtraction with an averaged spectrum, a two-dimensional spectrum with one-dimensional beam scan (Fig. 4A) can be described as

$$\begin{aligned}I(k_j, t) &= |p(k_j, t)|^2 + p(k_j, t)r^*(k_j) \exp\left[i\left(t\frac{\pi}{2}\right)\right] \\ &+ c.c.,\end{aligned}\quad (3)$$

where $p(k_j, t)$ is the electric field of the light on the line camera that is backscattered from the tissue at the lateral scanning position $x(t)$. r indicates the field of the reference light. It is Fourier transformed along the time axis t .

$$\begin{aligned}\mathcal{F}_t[I(k_j, t)](n) &= \mathcal{F}_t[|p(k_j, t)|^2](n) \\ &+ \mathcal{F}_t[p(k_j, t)r^*(k_j)](n) \otimes \delta(n f_A/N_A - f_A/4) \\ &+ \mathcal{F}_t[p^*(k_j, t)r(k_j)](n) \otimes \delta(n f_A/N_A + f_A/4),\end{aligned}\quad (4)$$

where $\mathcal{F}_t[\cdot](n)$ denotes the discrete Fourier transform from the time domain to the temporal frequency domain and \otimes is the convolution operator. $f_A = 1/T$ is the line rate of the camera, and the number of spectra, N_A , is obtained for one image. The first term of Eq. (4) and residual error of the spectrum subtraction are appeared as the central peak as in Fig. 4B. Since the phase of the fringes are modulated along the time axis by using the EOM with a step of $\pi/2$ radian, the complex interferometric signal and its complex conjugate corresponding to second and third terms in Eq. (4) are separated in the temporal frequency domain. One of them is clipped out

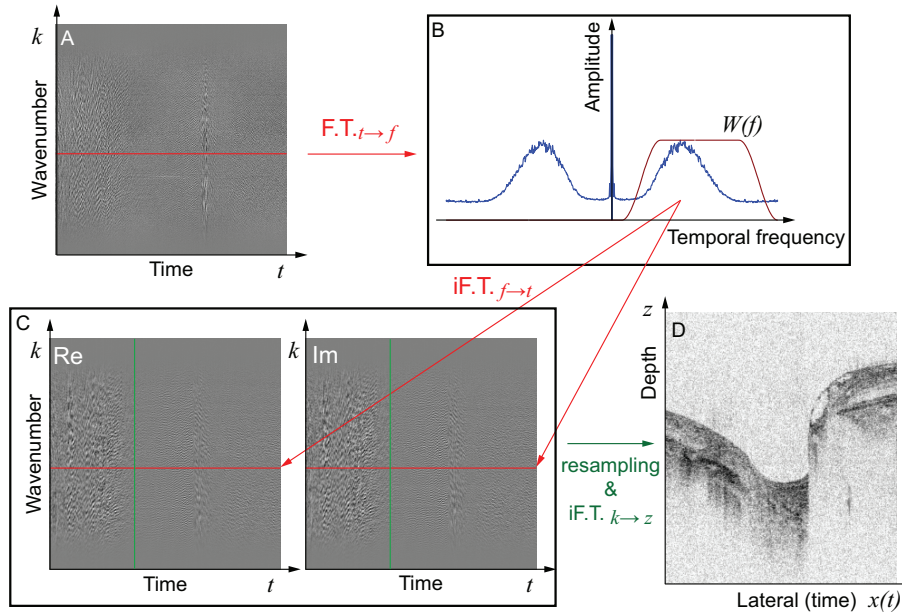


Fig. 4. The procedure to obtain the complex spectrum. The 2D spectral fringe (A) is Fourier transformed along the temporal axis t . The complex spectrum (C) is obtained by inverse Fourier transform the frequency spectrum (B) multiplied with the filter $W(f)$. After the spectrum resampling, dispersion compensation, and Fourier transform along the wavenumber axis k , the OCT image (D) is constructed.

by multiplying a window function $W(f)$. Then, it is inverse Fourier transformed to achieve the complex 2D spectrum I' (Fig. 4C).

$$I'(k_j, t) = p(k_j, t) r^*(k_j) \exp \left[i \left(l \frac{\pi}{2} \right) \right]. \quad (5)$$

After resampling (Sec. 2.2), we apply the iterative dispersion compensation method and inverse FFT from the k -axis to the z -axis, in order to reconstruct the complex-ambiguity-free image (Fig. 4D).

2.4. Performance of the system

To characterize the system performance, the fiber of the sample arm is reconnected to a reflector, as shown in Fig. 1 (broken line). Several axial scans with several delays are obtained and these axial profiles are shown in Fig. 5. The complex conjugate signals are broadened by the twofold effect of the dispersion mismatch because of the numerical dispersion compensation. They are removed via BM-scan method (Fig. 5B) and a depth range of 5.7 mm in air (4.2 mm in tissue) is achieved. The axial resolution was measured in these profiles by the following method. The number of sampling points was increased from 1,024 to 16,384 by zero padding before the Fourier transform. The mean full width at half maximum of the peak was measured to be 7.4 μm in tissue. The discrepancy from the expected resolution of 5.6 μm is perhaps due to the non-Gaussian shape of the source spectrum and the wavelength dependency of optical components.

The shot-noise-limited sensitivity is estimated as 108.7 dB by introducing the sample beam with a power of 1.37 mW to the reflector. Since the detector noise is relatively higher than the noise of silicon-based CCD camera, the expected sensitivity considering the camera noise

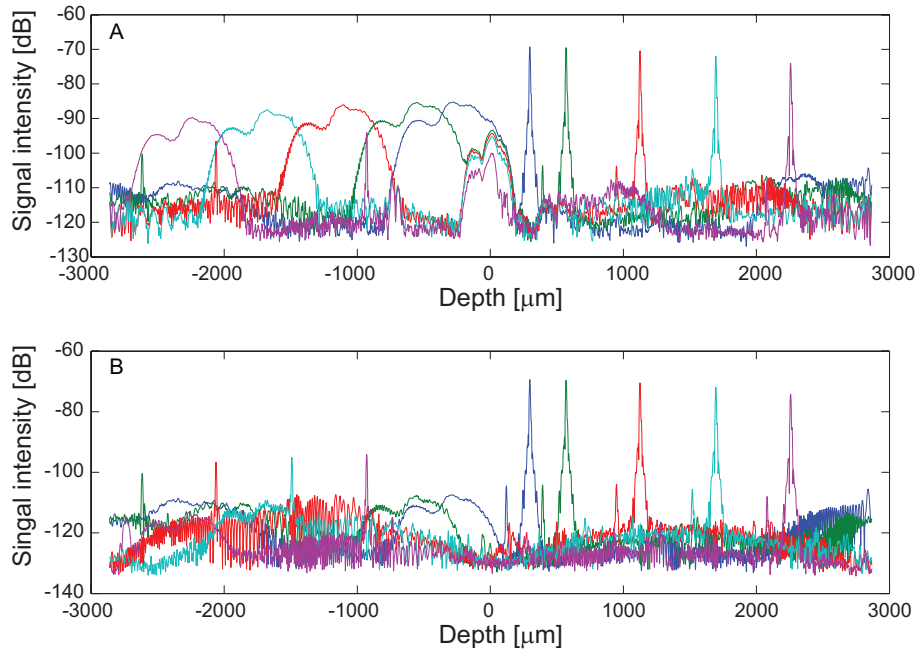


Fig. 5. The axial profile of OCT signals of the reflector in the sample arm at different delays with (A) conventional SD-OCT processing and (B) full-range imaging. The complex conjugate signals are broadened due to the large dispersion mismatch.

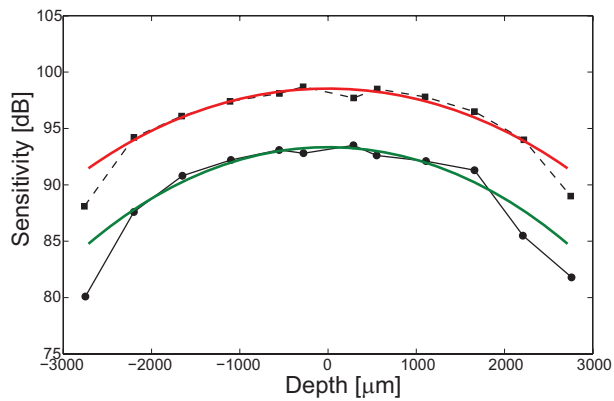


Fig. 6. The depth dependent sensitivity measured with a reflector. The measured sensitivity (circle, solid line); the measured sensitivity with full-range imaging (square, broken line); and fitted curves of theoretical signal decay (red and green lines).

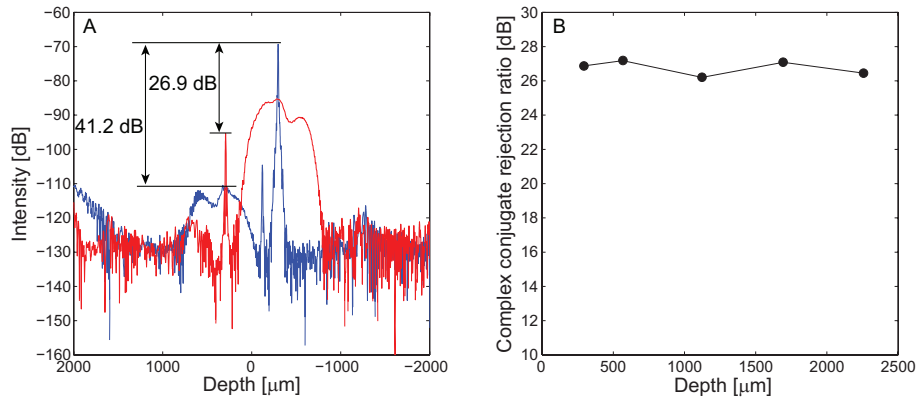


Fig. 7. The complex conjugate rejection ratio is determined by (A) comparing the signal intensities with the dispersion compensation (blue) and opposite dispersion compensation (red). (B) The rejection ratio as a function of depth.

and intensity noise of the light source is calculated as 103.4 dB with the optimal reference power. Currently, the sample beam is unpolarized, while the reference beam is polarized by the linear polarizer in the reference arm; thus, half of the sample beam power is lost. Moreover, the light power is reduced by approximately -2.2 dB when it is recoupled into the fiber optics. Consequently, the system sensitivity is predicted as 98.2 dB.

Figure 6 shows the depth dependent sensitivity of the system with/without the BM-scan method. The results are fitted by the theoretical sensitivity decay curves [34]. The offsets of the fitting curves are 93.4 and 98.5 dB. There is a sensitivity gain in full-range imaging since the BM-scan method functions as a bandpass filtering. The offset difference of the fitting curves is 5.1 dB.

In the practical system, the sensitivity is predicted as 94 dB with the probing power of 840 μ W from the optical loss of the retinal scanner -2.27 dB. This reduction may come from vignetting due to the small diaphragm and reflections at several optical components in the retinal scanner.

To define the complex conjugate rejection ratio (CCRR), full-range axial profiles are obtained by applying the dispersion compensation and opposite compensation (Fig. 7A). Then, the peak values of the OCT signals and their complex conjugates are compared. The depth-dependent CCRR is shown in Fig. 7B. It shows that the depth dependence of the CCRR is almost constant. The mean of CCRR is 26.8 ± 0.4 dB. Furthermore, in practical imaging, the dispersion compensation is applied to sharpen a OCT image; its mirror image is blurred. The intensity ratio of the signal to its complex conjugate is larger than the CCRR, e.g., ~ 41.2 dB in this particular experiment.

3. *In vivo* posterior eye imaging

The human macula lutea is scanned with the developed system. The image is shown in Fig. 8. The imaging range is 6×1.6 mm (lateral \times axial). The dynamic range of the image is 40 dB (-5 dB to 35 dB from noise floor). The dashed orange line indicates the zero-delay. Several layers in the retina are clearly visualized with high axial resolution. The external limiting membrane is observed too.

The volumetric imaging is performed in an area of 3×3 mm with axial scans of 1024×128 . The imaging time is 3.4 s per volume.

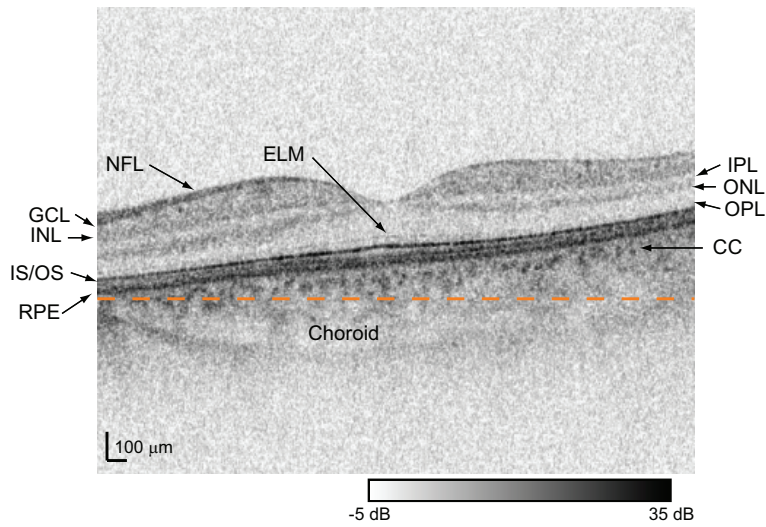


Fig. 8. The cross section of the macula lutea *in vivo* human eye. Several layers of the retina including the external limiting membrane are visualized with a high axial resolution. NFL: the nerve fiber layer, GCL: ganglion cell layer, INL: inner nuclear layer, IPL: inner plexiform layer, ONL: outer nuclear layer, OPL: outer plexiform layer, ELM: external limiting membrane, IS/OS: inner/outer segment junction, RPE: retinal pigment epithelium, CC: choriocalcarius. The orange dashed line denotes the zero-delay.

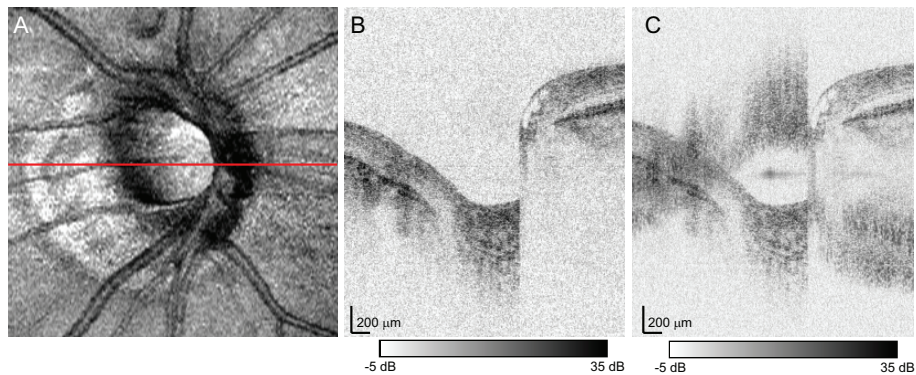


Fig. 9. The volumetric imaging result of the ONH. The red line in (A) the projection image denotes the scanning position of (B) (2.8 MB) the full-range cross-sectional image and (C) the cross section with conventional SD-OCT processing. The imaging size is 3×3 mm (1024×128 lines) in the lateral directions and 2.4 mm along the axial direction in tissue.

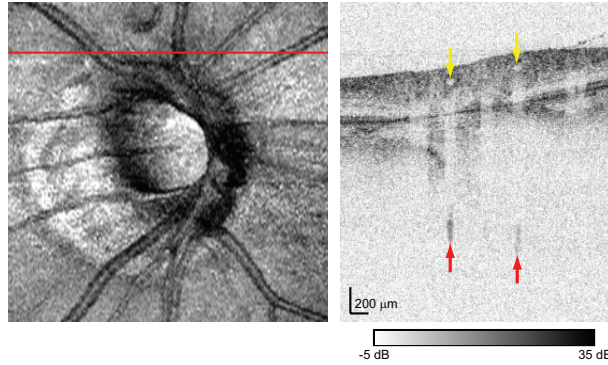


Fig. 10. Blood flow artifacts due to high flow speed (red arrows). Corresponding blood vessels are shown with low intensity (yellow arrows).

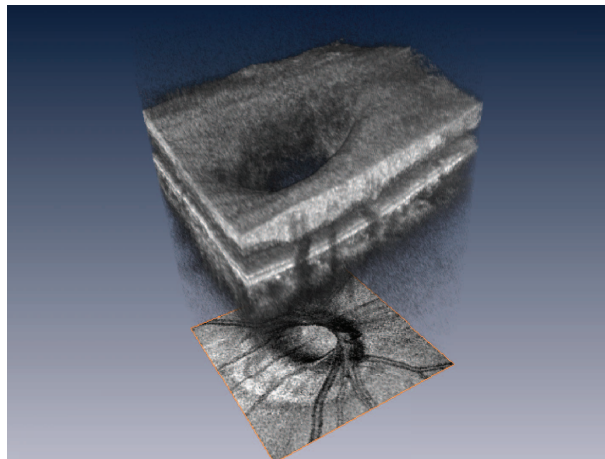


Fig. 11. (2.3 MB) The volume rendering image of the ONH.

Figure 9 shows the cross-sectional images of the ONH (31 y/o male, right eye). With the conventional imaging, the mirror image disturbs the OCT images. By applying the BM-scan method, the structure of the deep cup is observed. In the sequence of cross sections, it is found that there is no missing frame due to sample motion, and *in vivo* three-dimensional full-range imaging is achieved. In some cross sections, small spots appear beneath the retinal blood vessels (Fig. 10). Because of the fast blood flow velocity of such large retinal vessels, the Doppler shift of the backscattered light from the blood in these vessels exceeds half the line rate, $f_A/2$. Thus, the mirror image is observed. Three-dimensional structure is shown in the volume rendering image (Fig. 11). The deep ranging depth covers the entire deep cup with high signal intensity.

In the other sample (27 y/o male, left eye), the pore structure at the lamina cribrosa is clearly visible (Fig. 12) because of the high penetration of the $1 \mu\text{m}$ probe beam.

4. Discussions

The BM-scan method includes the effect of bandpass filtering. Thus, provides the sensitivity gain since the signal is concentrated but the noise is distributed in temporal frequency domain

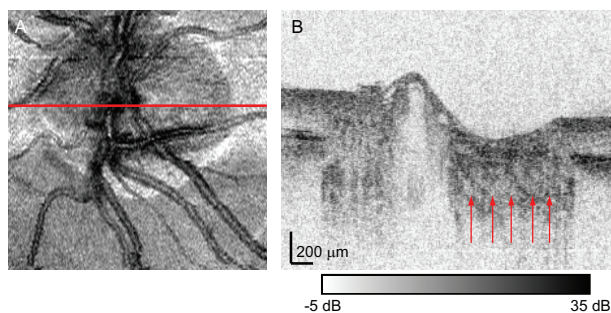


Fig. 12. The *en face* projection (A) and cross section (B) of the ONH. The laminar pores are clearly visualized (red arrows). The imaging size is 3×3 mm (1024×128 lines) in the lateral directions and 1.6 mm along the axial direction in tissue.

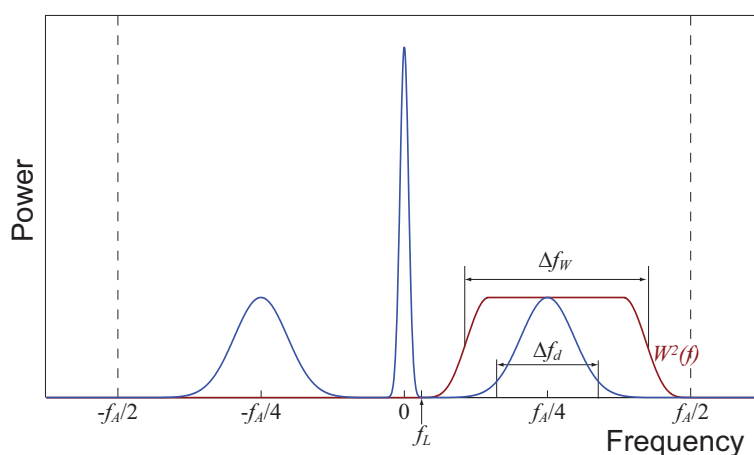


Fig. 13. The schematics of the power spectra of the OCT signal (green curve) and the window function (blue curve) in the temporal frequency domain. f_A : the line rate of the camera, f_L : lower cutoff frequency of the filter, Δf_w : filter bandwidth (FWHM), f_d : signal bandwidth ($1/e^2$).

[35]. This gain depends on the shape of the filter as follows:

$$G = \frac{f_A}{\int_{-f_A/2}^{f_A/2} W^2(f) df}, \quad (6)$$

where $0 \leq W(f) \leq 1$ denotes the window function used for Fourier filtering and f_A is the sampling rate of the spectrum. Here the noise is assumed to be white noise. This assumption is reasonable because, in the detection band of SD-OCTs (0 Hz to over 10 kHz), the flicker noise is ignorable comparing to the total noise power [36], and the frequency dependence of intensity noise of a light source will be quite low. In our case, the flat-topped window function is used.

It can be described as:

$$W(f) = \begin{cases} 0 & f < f_L \\ \frac{1}{2} - \frac{1}{2} \cos \left[2\pi \frac{f-f_L}{(1-R)(f_A/2-f_L)} \right] & f_L \leq f < f_L + \frac{(1-R)(f_A/2-f_L)}{2} \\ 1 & f_L + \frac{(1-R)(f_A/2-f_L)}{2} \leq f < f_L + \frac{(1+R)(f_A/2-f_L)}{2} \\ \frac{1}{2} + \frac{1}{2} \cos \left[2\pi \frac{f-f_L-(1+R)(f_A/2-f_L)/2}{(1-R)(f_A/2-f_L)} \right] & f_L + \frac{(1+R)(f_A/2-f_L)}{2} \leq f < f_A/2 \\ 0 & f \geq f_A/2, \end{cases} \quad (7)$$

where f_L is the lower cutoff frequency and R is the ratio of the flat-top region to the entire width of the window. In our case, $f_L = 1.15$ kHz and $R = 0.5$. By substituting these values into Eq. (7) and using Eq. (6), the sensitivity gain is estimated as 4.9 dB. This theoretically expected gain is in good agreement with the experimental results, i.e., 5.1 dB.

One of the limitations of the BM-scan method is the requirement of the dense scanning step comparing to the beam spot size on the tissues because the bandwidth of the point spread function should be narrower than the filter bandwidth Δf_w . By assuming a Gaussian amplitude distribution and a constant scanning velocity of the sample beam, the maximum bandwidth of the signal ($1/e^2$ in power spectrum) can be described as

$$\Delta f_d = \frac{4f_A \Delta x}{\pi d}, \quad (8)$$

where d is the $1/e^2$ beam spot diameter and Δx indicates the lateral separation between neighboring sampling points. Figure 13 shows the relationship between the temporal frequency domain signal power and the window function. Due to phase modulation, the signal band is shifted by $f_A/4$. To achieve full-range imaging, the condition $\Delta f_d < \Delta f_w \leq f_A/2$ should be satisfied. It can be rewritten to $\Delta x/d < \pi \Delta f_w / 4f_A < \pi/8$. In our system, $\Delta x = \sim 3 \mu\text{m}$, $d = \sim 20 \mu\text{m}$, and $f_A = 38.3$ kHz; and, the signal bandwidth Δf_d is estimated as 7.1 kHz. Finally, the FWHM bandwidth of the window function is determined to be 12.3 kHz to maintain the tolerance for the sample motion.

The axial motion causes the Doppler frequency shift, resulting in the shift of the signal band. When the signal band exceeds the filter band, the signal drop occurs. In our case, the margins between the widest signal band and the filter band are -1.45 and $+3.75$ kHz. They correspond to axial velocities of -0.76 and $+1.95$ mm/s. A larger Doppler frequency shift than $f_A/4 - \Delta f_d/2$ will result in the residual conjugate signals. The high acquisition rate mitigates this phenomenon, and due to the high-speed line scan camera, our method is stable even for *in vivo* retinal imaging.

Figure 14 shows the full-range cross sections obtained by applying the BM-scan method and the least-squares algorithm for phase shifting interferometry [37]. The residual mirror image due to sample motion is appeared remarkably when the least-squares method is applied with four frames (Fig. 14A, black arrow), and slightly observed with five frames (Fig. 14B, black arrow). In contrast, the mirror image is not observed when we use the BM-scan method (Fig. 14A). This shows that the BM-scan method is more tolerant of the sample motion than the least-squares method. This is maybe due to the relatively wide frequency band of BM-scan method in comparison to that of the least-squares method.

5. Conclusions

The full-range, high-speed $1 \mu\text{m}$ SD-OCT system has been developed. The BM-scan method is introduced with the discrete phase modulation. The fringe washout due to phase modulation is ignored, and the sensitivity gain of 5.1 dB is obtained by the BM-scan method. The influence

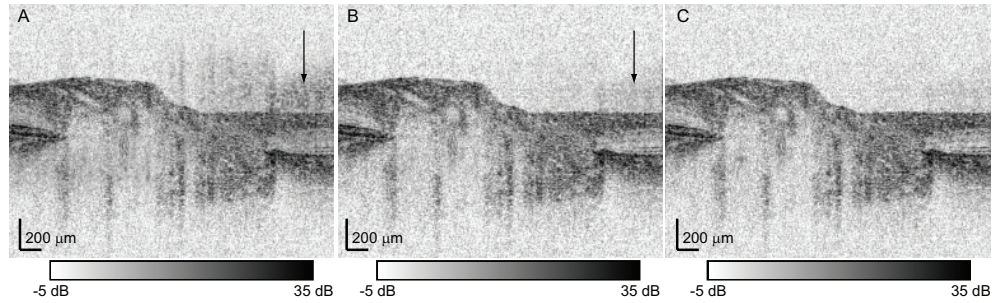


Fig. 14. Comparison of full-range images by using the least-squares method with (A) four frames and (B) five frames, and (C) BM-scan method.

of the large systematic dispersion mismatch is excluded in the new spectrometer calibration algorithm. By using this system, high-penetration, high-resolution *in vivo* volumetric imaging of the retina and choroid is performed for normal eyes. Full-range imaging with high tolerance for the volunteer's head movement is achieved due to high-speed acquisition. The resulting deep ranging depth due to full-range imaging enables the morphological imaging of the deep cup in the ONH.

Acknowledgment

This research is supported by a Grant-in-Aid for Scientific Research 18360029 and JSPS fellows 18-3827 from the Japan Society for the Promotion of Science (JSPS), Japan Science and Technology Agency, and the Special Research Project of Nanoscience at the University of Tsukuba. Shuichi Makita is a JSPS research fellow. The authors acknowledge Hamamatsu Photonics K.K. which provided the prototype high-speed InGaAs line scan camera.